INTERNATIONAL JOURNAL FOR NUMERICAL METHODS IN FLUIDS
Int. J. Numer. Meth. Fluids 2010; **62**:237–266
Published online 26 February 2009 in Wiley InterScience (www.interscience.wiley.com). DOI: 10.1002/fld.2013

A streamfunction–velocity approach for 2D transient incompressible viscous flows‡

Jiten C. Kalita[1,*,†,§] and Murli M. Gupta[2,¶]

[1]*Department of Mathematics, Indian Institute of Technology, Guwahati 781039, India*
[2]*Department of Mathematics, The George Washington University, Washington, DC 20052, U.S.A.*

SUMMARY

We recently proposed (*J. Comput. Phys.* 2005; **207**(1):52–68) a new paradigm for solving the steady-state two-dimensional (2D) Navier–Stokes (N–S) equations using a streamfunction–velocity (ψ–v) formulation. This formulation was shown to avoid the difficulties associated with the traditional formulations (primitive variables and streamfunction-vorticity formulations). The new formulation was found to be second-order accurate and was found to yield accurate solutions of a number of fluid flow problems.

In this paper, we extend the ideas and propose a second-order implicit, unconditionally stable ψ–v formulation for the unsteady incompressible N–S equations. The method is used to solve several 2D time-dependent fluid flow problems, including the flow decayed by viscosity problem with analytical solution, the lid-driven square cavity problem, the backward-facing step problem and the flow past a square prism problem. For the problems with known exact solutions, our coarse grid transient solutions are extremely close to the analytical ones even for high Reynolds numbers (Re). For the driven cavity problem, our time-marching steady-state solutions up to $Re = 7500$ provide excellent matches with established numerical results, and for $Re = 10\,000$, our study concludes that the asymptotic stable solution is periodic as has been found by other authors in recent studies. For the backward step problem, our numerical results are in excellent agreement with established numerical and experimental results. Finally, for the flow past a square prism, we have very successfully simulated the von Kármán vortex street for $Re = 200$.

Received 11 June 2008; Revised 5 January 2009; Accepted 11 January 2009

KEY WORDS: transient; streamfunction–velocity formulation; Navier–Stokes equations; finite differences; computationally efficient; von Kármán street

*Correspondence to: Jiten C. Kalita, Department of Mathematics, Indian Institute of Technology, Guwahati 781039, India.
†E-mail: jiten@iitg.ernet.in
‡Supporting information may be found in the online version of this article.
§Associate Professor.
¶Professor.

1. INTRODUCTION

The non-dimensional unsteady two-dimensional (2D) Navier–Stokes equations for incompressible viscous flows in the primitive variable formulation are given by

$$\frac{\partial u}{\partial x}+\frac{\partial v}{\partial y}=0 \tag{1}$$

$$\frac{\partial u}{\partial t}+u\frac{\partial u}{\partial x}+v\frac{\partial u}{\partial y}=-\frac{\partial p}{\partial x}+\frac{1}{Re}\nabla^2 u \tag{2}$$

$$\frac{\partial v}{\partial t}+u\frac{\partial v}{\partial x}+v\frac{\partial v}{\partial y}=-\frac{\partial p}{\partial y}+\frac{1}{Re}\nabla^2 v \tag{3}$$

where t is the time, u, v are velocities along the x-and y-directions, respectively, p represents the pressure and Re is the non-dimensional Reynolds number. The direct solution of this formulation has traditionally been difficult due to the presence of the pressure term in Equations (2)–(3). An alternative formulation using streamfunction ψ and vorticity ω has been used for several decades:

$$\omega_t-\frac{1}{Re}(\omega_{xx}+\omega_{yy})+(u\omega_x+v\omega_y)=0 \tag{4}$$

$$\nabla^2\psi=\psi_{xx}+\psi_{yy}=-\omega(x,y) \tag{5}$$

The velocities are defined as

$$u=\psi_y \quad \text{and} \quad v=-\psi_x \tag{6}$$

and the vorticity is defined by

$$\omega=v_x-u_y \tag{7}$$

This ψ–ω formulation has been quite successful and has been used by a large number of researchers over the past several decades to test new methods for the numerical solutions of a variety of fluid flow problems. The typical difficulty with this formulation is the fact that the vorticity ω is not defined at the no-slip boundaries; ω is defined through the Poisson Equation (5) that needs to be solved on the boundaries so that boundary values of ω can be specified for the vorticity transport Equation (4) when this formulation is utilized. However, the values of ω on the boundaries are generally unspecified and one needs to carry out a variety of numerical approximations in order to specify these boundary values.

A plethora of numerical schemes exist for solving the N–S equations both in the primitive variable and in the ψ–ω form [1–13]. An alternative approach of the streamfunction–velocity (ψ–v) formulation was recently proposed by the authors [14, 15] for the steady-state Navier–Stokes equations. This formulation is of second-order accuracy and carries streamfunction and velocities as the variables. The boundary conditions for streamfunction and velocity are generally known in fluid flow problems, are easy to implement computationally, and this formulation has been found to be very efficient. We have also proposed a spatially fourth-order accurate variant of this scheme in [15]. It may be noted that while dealing with the ψ–v formulation of the N–S equations,

DOI: 10.1002/fld

the velocities appearing in the advective terms as well as those coming from the derivatives of ψ become an integral part of the computational procedure in our formulation [14, 15]. Thus the velocities need not be approximated in our formulation. A similar approach, called the biharmonic formulation, was also proposed by a number of authors [16–18]. Both of these formulations remove the pressure p and vorticity ω as a part of the computational procedure and this results in a computationally efficient procedure. We note that our ψ–v formulations differ significantly from the pure-streamfunction approach in that the coefficient matrices resulting from the discretization of the ψ-only approach are more complicated than those resulting from our ψ–v formulation.

In the present paper, we continue the new paradigm and apply our methodology to the unsteady 2D N–S equations. The proposed method is implicit, unconditionally stable, and we show that this formulation is computationally more efficient than most of the existing schemes for solving the time-dependent incompressible N–S equations. We have used the new formulation to solve five time-dependent fluid flow problems: (i) the transient flow decayed by viscosity; (ii) the problem with a non-homogeneous source term; (iii) the famous lid-driven cavity problem; (iv) the backward-facing step problem and (v) the motion past a square prism problem. The first two problems have known analytical solutions and detailed comparisons of errors are possible in those cases.

The robustness of our method is apparent when we apply it to the lid-driven cavity and the backward-facing step problems. In the case of the lid-driven cavity problem, our method is able to very accurately capture the almost periodic nature of the asymptotic solution for $Re = 10\,000$. The power of our scheme is better realized when the severe test case of flow past a square prism is computed and the famous von Kármán street is simulated very successfully.

It is a well-known fact that the ψ–ω formulation, despite being a very popular approach for solving the 2D N–S equations, cannot be applied in the 3D case. However, it is possible to compute flows governed by the 3D N–S equations using the vector form of the ψ–ω formulation [19]. With the development of the proposed scheme for the biharmonic form of the transient N–S equations, it will now be possible to extend this approach to compute 3D flows as well. This paper ends with a brief discussion on that.

This paper is organized into six sections. In Section 2, we describe the derivations of transient streamfunction–velocity formulations. In Section 3, we perform a linear stability analysis for this formulation, and discuss the computational considerations in Section 4. We present the detailed results of our computations in Section 5, and offer a few conclusions in Section 6. As mentioned in the previous paragraph, we briefly discuss the extension of our scheme to the 3D N–S equations in the Appendix.

2. MATHEMATICAL FORMULATION AND DISCRETIZATION

In our previous paper [14], we introduced a new paradigm for solving the steady-state Navier–Stokes equations in the form

$$\nabla^4\psi - Re(v\nabla^2 u - u\nabla^2 v) = f \tag{8}$$

in a convex domain Ω with boundary $\partial\Omega$. (Here, u, v, ψ and f are functions of x, y and Re is the Reynolds number.) This equation can be obtained from the steady-state form of (4) by substituting the value of ω with the help of Equation (5). The second-order compact formulation for (8) on a

DOI: 10.1002/fld

uniform grid of step-length h in both x- and y-directions is given by

$$\begin{aligned}&\psi_{i-1,j-1}-8\psi_{i,j-1}+\psi_{i+1,j-1}-8\psi_{i-1,j}+28\psi_{i,j}-8\psi_{i+1,j}+\psi_{i-1,j+1}-8\psi_{i,j+1}\\&+\psi_{i+1,j+1}-3h(u_{i,j-1}-u_{i,j+1}+v_{i+1,j}-v_{i-1,j})-0.5Reh^2\{v_{i,j}(u_{i+1,j}+u_{i-1,j}\\&+u_{i,j+1}+u_{i,j-1})-u_{i,j}(v_{i+1,j}+v_{i-1,j}+v_{i,j+1}+v_{i,j-1})\}=\frac{h^4}{2}f_{i,j}\end{aligned}\tag{9}$$

This formulation carries the streamfunction ψ and velocities u, v as variables and uses only the nearest neighbors in the compact cell $(x_{i\pm1}, y_{j\pm1})$ centered at the grid point (x_i, y_j). This formulation has the trunction error of order h^2.

The velocities may be computed by the standard second-order formulas:

$$u_{i,j}=\frac{1}{2h}(\psi_{i,j+1}-\psi_{i,j-1})\tag{10}$$

$$v_{i,j}=-\frac{1}{2h}(\psi_{i+1,j}-\psi_{i-1,j})\tag{11}$$

Fourth-order approximations for velocities are also available [14]:

$$u_{i,j}=\frac{3}{4h}(\psi_{i,j+1}-\psi_{i,j-1})-\frac{1}{4}(u_{i,j+1}+u_{i,j-1})\tag{12}$$

$$v_{i,j}=-\frac{3}{4h}(\psi_{i+1,j}-\psi_{i-1,j})-\frac{1}{4}(v_{i+1,j}+v_{i-1,j})\tag{13}$$

Making use of Equation (5), the time-dependent Navier–Stokes Equations (4) may be written as

$$\nabla^4\psi-Re(v\nabla^2u-u\nabla^2v)=Re\left[\frac{\partial}{\partial t}(\nabla^2\psi)\right]\tag{14}$$

Using forward differences for the time derivative and using Equation (9), an implicit finite difference approximation for Equation (14) may be written as

$$\begin{aligned}&0.5Reh^2[\psi_{i+1,j}^{(n+1)}+\psi_{i-1,j}^{(n+1)}+\psi_{i,j+1}^{(n+1)}+\psi_{i,j-1}^{(n+1)}-4\psi_{i,j}^{(n+1)}]\\&=0.5Reh^2[\psi_{i+1,j}^{(n)}+\psi_{i-1,j}^{(n)}+\psi_{i,j+1}^{(n)}+\psi_{i,j-1}^{(n)}-4\psi_{i,j}^{(n)}]\\&\quad+\Delta t[\psi_{i-1,j-1}^{(n)}-8\psi_{i,j-1}^{(n)}+\psi_{i+1,j-1}^{(n)}\\&\quad-8\psi_{i-1,j}^{(n)}+28\psi_{i,j}^{(n)}-8\psi_{i+1,j}^{(n)}+\psi_{i-1,j+1}^{(n)}-8\psi_{i,j+1}^{(n)}\\&\quad+\psi_{i+1,j+1}^{(n)}-3h(u_{i,j-1}^{(n)}-u_{i,j+1}^{(n)}+v_{i+1,j}^{(n)}-v_{i-1,j}^{(n)})\\&\quad-0.5Reh^2\{v_{i,j}^{(n)}(u_{i+1,j}^{(n)}+u_{i-1,j}^{(n)}+u_{i,j+1}^{(n)}+u_{i,j-1}^{(n)})\\&\quad-u_{i,j}^{(n)}(v_{i+1,j}^{(n)}+v_{i-1,j}^{(n)}+v_{i,j+1}^{(n)}+v_{i,j-1}^{(n)})\}]\end{aligned}\tag{15}$$

This formulation is $O(h^2, \Delta t)$ accurate. Here, the superscripts (n) and $(n+1)$ represent the values at the n- and $(n+1)$th time levels, respectively. A more general formulation is obtained by using

DOI: 10.1002/fld

a weighted time average parameter μ such that $t_\mu=(1-\mu)t^{(n)}+\mu t^{(n+1)}$ for $0\leqslant\mu\leqslant1$ as

$$
\begin{aligned}
&0.5Reh^2[\psi_{i+1,j}^{(n+1)}+\psi_{i-1,j}^{(n+1)}+\psi_{i,j+1}^{(n+1)}+\psi_{i,j-1}^{(n+1)}-4\psi_{i,j}^{(n+1)}]\\
&=0.5Reh^2[\psi_{i+1,j}^{(n)}+\psi_{i-1,j}^{(n)}+\psi_{i,j+1}^{(n)}+\psi_{i,j-1}^{(n)}-4\psi_{i,j}^{(n)}]\\
&\quad+\Delta t(1-\mu)[\psi_{i-1,j-1}^{(n)}-8\psi_{i,j-1}^{(n)}+\psi_{i+1,j-1}^{(n)}\\
&\quad-8\psi_{i-1,j}^{(n)}+28\psi_{i,j}^{(n)}-8\psi_{i+1,j}^{(n)}+\psi_{i-1,j+1}^{(n)}-8\psi_{i,j+1}^{(n)}\\
&\quad+\psi_{i+1,j+1}^{(n)}-3h(u_{i,j-1}^{(n)}-u_{i,j+1}^{(n)}+v_{i+1,j}^{(n)}-v_{i-1,j}^{(n)})\\
&\quad-0.5Reh^2\{v_{i,j}^{(n)}(u_{i+1,j}^{(n)}+u_{i-1,j}^{(n)}+u_{i,j+1}^{(n)}+u_{i,j-1}^{(n)})\\
&\quad-u_{i,j}^{(n)}(v_{i+1,j}^{(n)}+v_{i-1,j}^{(n)}+v_{i,j+1}^{(n)}+v_{i,j-1}^{(n)})\}]\\
&\quad+\Delta t\mu[\psi_{i-1,j-1}^{(n+1)}-8\psi_{i,j-1}^{(n+1)}+\psi_{i+1,j-1}^{(n+1)}\\
&\quad-8\psi_{i-1,j}^{(n+1)}+28\psi_{i,j}^{(n+1)}-8\psi_{i+1,j}^{(n+1)}+\psi_{i-1,j+1}^{(n+1)}-8\psi_{i,j+1}^{(n+1)}\\
&\quad+\psi_{i+1,j+1}^{(n+1)}-3h(u_{i,j-1}^{(n+1)}-u_{i,j+1}^{(n+1)}+v_{i+1,j}^{(n+1)}-v_{i-1,j}^{(n+1)})\\
&\quad-0.5Reh^2\{v_{i,j}^{(n+1)}(u_{i+1,j}^{(n+1)}+u_{i-1,j}^{(n+1)}+u_{i,j+1}^{(n+1)}+u_{i,j-1}^{(n+1)})\\
&\quad-u_{i,j}^{(n+1)}(v_{i+1,j}^{(n+1)}+v_{i-1,j}^{(n+1)}+v_{i,j+1}^{(n+1)}+v_{i,j-1}^{(n+1)})\}]
\end{aligned}
\tag{16}
$$

Varying the values of μ provides a class of Navier–Stokes integrators, for example, for $\mu=0.5$, we have Crank–Nicolson type scheme with truncation error of order $O(h^2,\Delta t^2)$. We note here that all of these computational stencils require grid values at nine points at both (n)th and $(n+1)$th time levels and as such may be labelled as a $(9,9)$ scheme.

3. LINEARIZED STABILITY ANALYSIS

We perform a von Neumann linear stability analysis by setting the terms not explicitly involving ψ in Equation (14) to zero. Equation (16) may be written as

$$[A]^{(n+1)}-2c\mu[B]^{(n+1)}=[A]^{(n)}-2c(1-\mu)[B]^{(n)} \tag{17}$$

where $A=\psi_{i+1,j}+\psi_{i-1,j}+\psi_{i,j+1}+\psi_{i,j-1}-4\psi_{ij}$, $B=28\psi_{ij}-8(\psi_{i+1,j}+\psi_{i-1,j}+\psi_{i,j+1}+\psi_{i,j-1})+(\psi_{i+1,j-1}+\psi_{i-1,j+1}+\psi_{i-1,j+1}+\psi_{i-1,j-1})$ and $c=\Delta t/(Reh^2)$ (>0). Let $\psi_{ij}^{(n)}=b^{(n)}\mathrm{e}^{Ii\theta_x}\mathrm{e}^{Ij\theta_y}$, where $b^{(n)}$ is the amplitude at time level n, $I=\sqrt{-1}$, and $\theta_x(=2\pi h/\Lambda_1)$ and $\theta_y(=2\pi h/\Lambda_2)$ are the phase angles with wavelengths Λ_1 and Λ_2, respectively. For stability, the amplification factor $\xi=b^{(n+1)}/b^{(n)}$ must satisfy

$$|\xi|^2-1\leqslant0 \tag{18}$$

DOI: 10.1002/fld

Substituting the expressions for $\psi_{ij}^{(n)}$ and $\psi_{ij}^{(n+1)}$ in Equation (17), we get

$$\begin{aligned}
&b^{(n+1)}[(e^{I\theta_x}+e^{-I\theta_x}+e^{I\theta_y}+e^{-I\theta_y}-4)-2c\mu\{28-8(e^{I\theta_x}+e^{-I\theta_x}+e^{I\theta_y}+e^{-I\theta_y})\\
&\quad+(e^{I(\theta_x+\theta_y)}+e^{I(\theta_x-\theta_y)}+e^{-I(\theta_x-\theta_y)}+e^{-I(\theta_x+\theta_y)})\}]\\
&=b^{(n)}[(e^{I\theta_x}+e^{-I\theta_x}+e^{I\theta_y}+e^{-I\theta_y}-4)+2c(1-\mu)\{28-8(e^{I\theta_x}+e^{-I\theta_x}+e^{I\theta_y}+e^{-I\theta_y})\\
&\quad+(e^{I(\theta_x+\theta_y)}+e^{I(\theta_x-\theta_y)}+e^{-I(\theta_x-\theta_y)}+e^{-I(\theta_x+\theta_y)})\}] \qquad (19)
\end{aligned}$$

Or

$$\begin{aligned}
\xi&=\frac{b^{(n+1)}}{b^{(n)}}\\
&=\frac{\cos\theta_x+\cos\theta_y-2-2c(1-\mu)\{14-8\cos\theta_x-8\cos\theta_y+\cos(\theta_x+\theta_y)+\cos(\theta_x-\theta_y)\}}{\cos\theta_x+\cos\theta_y-2-2c\mu\{14-8\cos\theta_x-8\cos\theta_y+\cos(\theta_x+\theta_y)+\cos(\theta_x-\theta_y)\}}\\
&=\frac{\{1+16c(1-\mu)\}(\cos\theta_x+\cos\theta_y)+4c(1-\mu)\cos\theta_x\cos\theta_y-\{28c(1-\mu)-2\}}{(1+16c\mu)(\cos\theta_x+\cos\theta_y)-4c\mu\cos\theta_x\cos\theta_y-(28c\mu+2)}\\
&=\frac{a+b}{a} \qquad (20)
\end{aligned}$$

where $a=(1+16c\mu)(\cos\theta_x+\cos\theta_y)-4c\mu\cos\theta_x\cos\theta_y-(28c\mu+2)$ and $b=-16c(\cos\theta_x+\cos\theta_y)+4c\cos\theta_x\cos\theta_y+28c$. As b is always non-negative (with a maximum value $64c$ and minimum value 0), for stability, Equation (18) is equivalent to $b+2a\leqslant 0$. We have the strictest stability criteria when $\cos\theta_x=\cos\theta_y=-1$ (as $b+2a$ will have the maximum for those values) when the stability criteria reduces to

$$(1-2\mu)\leqslant\frac{1}{8c}$$

which is always true if $\mu\geqslant\frac{1}{2}$. Thus our scheme is unconditionally stable for $\frac{1}{2}\leqslant\mu\leqslant 1$ and as such, the $O(\Delta t^2, h^2)$ scheme corresponding to $\mu=\frac{1}{2}$ given by Equation (16) is unconditionally stable.

4. SOLUTION OF ALGEBRAIC SYSTEMS

We now discuss the solution of algebraic systems associated with the proposed finite difference approximations. The system of equations resulting from Equation (16) can be written in the matrix form as

$$A\boldsymbol{\Psi}^{(n+1)}=\mathbf{f}(\boldsymbol{\Psi}^{(n)},\mathbf{u}^{(n)},\mathbf{v}^{(n)},\mathbf{u}^{(n+1)},\mathbf{v}^{(n+1)}) \qquad (21)$$

where the coefficient matrix A is an asymmetric sparse matrix. For a grid of size $m\times n$, A has dimension $mn\times mn$, and $\boldsymbol{\Psi}^{(n+1)}$, $\boldsymbol{\Psi}^{(n)}$, $\mathbf{f}$, $\mathbf{u}^{(n)}$, $\mathbf{v}^{(n)}$, $\mathbf{u}^{(n+1)}$, $\mathbf{v}^{(n+1)}$ are vectors with mn components. Once Equation (21) is solved for discrete values of streamfunction ψ, the velocities u, v can

DOI: 10.1002/fld

be obtained from the fourth-order approximations (12) and (13), or by the second-order central difference approximations (10) and (11). The velocity Equations (12) and (13) yield tridiagonal linear systems, which can be solved directly.

We note that Equation (21) contains the $(n+1)$th time level velocities, which are available only after the streamfunction is available at the $(n+1)$th time level. Here we adopt a local linearization strategy (called Strategy 1) for which the algorithm is defined as follows:

1. Initialize $\boldsymbol{\Psi}^{(n+1)}$, $\mathbf{u}^{(n+1)}$ and $\mathbf{v}^{(n+1)}$ (with $\boldsymbol{\Psi}^{(n)}$, $\mathbf{u}^{(n)}$, $\mathbf{v}^{(n)}$).
2. Set $\boldsymbol{\Psi}_{\text{old}}^{(n+1)} = \boldsymbol{\Psi}^{(n+1)}$.
3. Compute $\boldsymbol{\Psi}^{(n+1)}$ using Equation (21).
4. Compute $\mathbf{u}^{(n+1)}$ and $\mathbf{v}^{(n+1)}$ using Equations (12), (13).
5. If $\max|\boldsymbol{\Psi}^{(n+1)} - \boldsymbol{\Psi}_{\text{old}}^{(n+1)}| <$ tolerance limit, then stop; else repeat steps 2–5 until convergence.

Another strategy (Strategy 2) is to calculate streamfunction ψ from the first-order time accurate scheme given in Equation (15), then calculating the $(n+1)$th time level values of the velocities u and v, and then using those values in Equation (21). With this strategy, at each time level, a corrector type of step is introduced that requires larger computational times. Owing to the fact that steps 2–5 in Strategy 1 have to run until convergence, Strategy 2 may still be computationally competitive. The fact that the proposed scheme (16) is unconditionally stable for $\frac{1}{2} \leqslant \mu \leqslant 1$ allows us to use large time steps. For steady-state problems where the steady state is reached through time marching, this can be very useful and computationally efficient.

The next step now is to solve Equation (21) using iterative methods. As the coefficient matrix A is generally not diagonally dominant, conventional iterative methods such as Gauss–Seidel are very slow to converge (or diverge). In order to solve these systems, we use the biconjugate gradient stabilized method (BiCGStab) [20–23] without preconditioning.

To solve the transient N–S equations using the proposed formulation, we employ an outer–inner iteration procedure. In a typical outer temporal cycle, we discretize Equation (14) using (16) and solve the resulting system of algebraic equations by BiCGStab. The BiCGStab constitutes the inner iteration cycles. Once (16) is solved, u and v are calculated using (12) and (13). This constitutes one outer iteration cycle. The stopping criteria for the inner iterations are different for different problems (see Sections 5.1 and 5.3). All of our computations were carried out on a Pentium 4-based PC with 512 MB RAM.

5. NUMERICAL EXAMPLES

In order to validate the proposed scheme and test its robustness, we apply it to five time-dependent fluid flow problems. These are (i) the transient flow decayed by viscosity, (ii) the problem with a non-homogeneous source term, (iii) the famous lid-driven cavity problem, (iv) the backward-facing step problem and (v) the motion past a square prism problem. The first two problems have known analytical solutions and detailed comparisons of errors are possible in those cases. Unless otherwise noted, zero initial data were used in all computations. It is worth mentioning that, since vorticity is not a part of our solution process, all of the results being presented for vorticity are obtained using Equation (7) through post-processing; we have used the standard second-order central difference formula for the derivatives appearing in (7).

DOI: 10.1002/fld

Table I. Problem 1: flow decayed by viscosity. Convergence rate of the numerical scheme with fourth-order velocity: maximum error comparisons on different grid sizes for u, v, ψ, and ω, $Re=10000$.

Grid		11×11	Rate	21×21	Rate	41×41
$t=1$	u_{er}	6.099×10^{-5}	4.046	3.691×10^{-6}	4.054	2.221×10^{-7}
	v_{er}	4.953×10^{-5}	3.906	3.303×10^{-6}	3.975	2.101×10^{-7}
	ψ_{er}	3.485×10^{-6}	4.523	1.516×10^{-7}	4.794	5.465×10^{-9}
	ω_{er}	2.969×10^{-2}	1.889	8.018×10^{-3}	1.973	2.043×10^{-3}
$t=5$	u_{er}	5.886×10^{-5}	4.004	3.668×10^{-6}	3.990	2.309×10^{-7}
	v_{er}	5.975×10^{-5}	3.921	3.942×10^{-6}	4.159	2.207×10^{-7}
	ψ_{er}	3.491×10^{-6}	4.552	1.488×10^{-7}	5.019	4.588×10^{-9}
	ω_{er}	2.968×10^{-2}	1.889	8.011×10^{-3}	1.973	2.041×10^{-3}

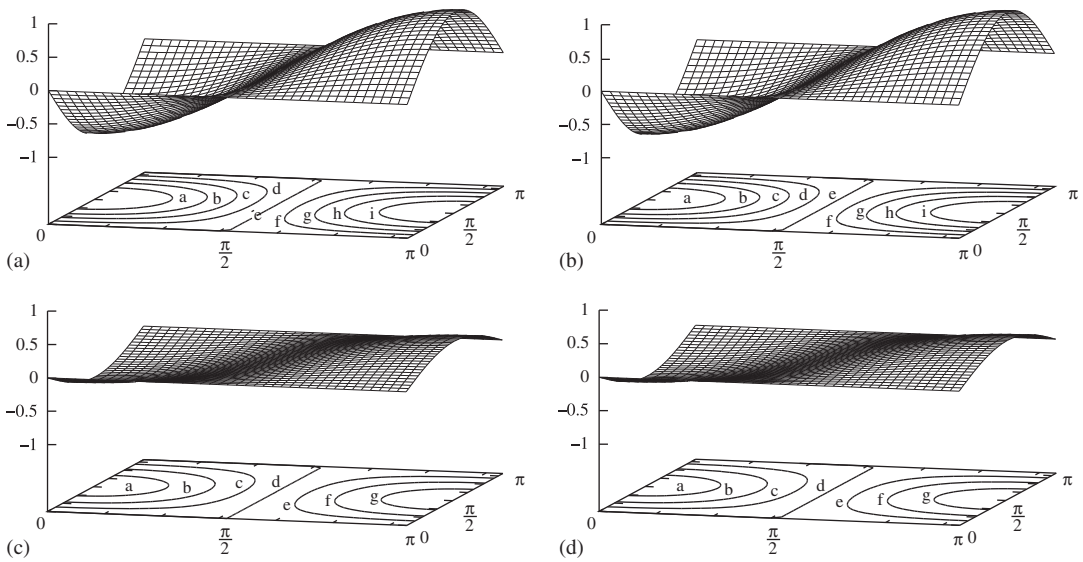

Figure 1. Problem 1: flow decayed by viscosity. Surface and contour plots u-velocity for ($Re=1000$, 41×41 grid, $\Delta t=0.01$): (a) numerical solution and (b) exact solution at $t=1$, (contour values: $a=-0.8$, $b=-0.6$, $c=-0.4$, $d=-0.2$, $e=0$, $f=0.2$, $g=0.4$, $h=0.6$, $i=0.8$) (c) numerical solution and (d) exact solution at $t=500$, contour values: ($a=-0.3$, $b=-0.2$, $c=-0.1$, $d=0$, $e=0.1$, $f=0.2$, $g=0.3$).

5.1. Problem 1: flow decayed by viscosity

We consider the problem of flow decayed by viscosity [1, 3, 13, 16, 24] which is governed by the 2D N–S Equations (1)–(3) in the square $0\leqslant x, y\leqslant\pi$, and has analytical solutions given by

$$u(x, y, t)=-\cos x\sin y\,\mathrm{e}^{-2t/Re},\quad v(x, y, t)=\sin x\cos y\,\mathrm{e}^{-2t/Re} \tag{22}$$

and

$$\psi(x, y, t)=(\cos x\cos y)\mathrm{e}^{-2t/Re} \tag{23}$$

The initial and boundary conditions for u, v and ψ can be found from (22) and (23).

DOI: 10.1002/fld

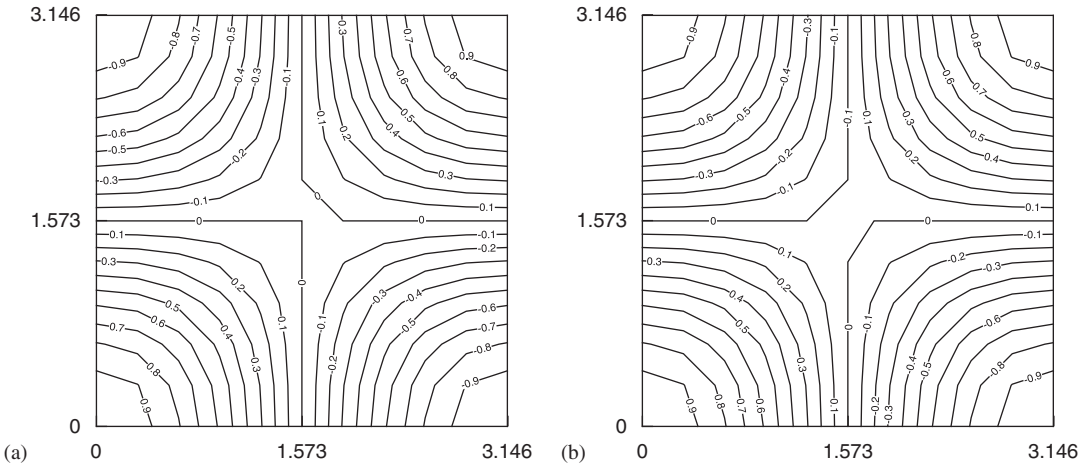

Figure 2. Problem 1: flow decayed by viscosity. Streamline contours at time $t=5$ obtained with $\Delta t=0.1$ and grid size 11×11 for $Re=10000$: (a) exact and (b) numerical.

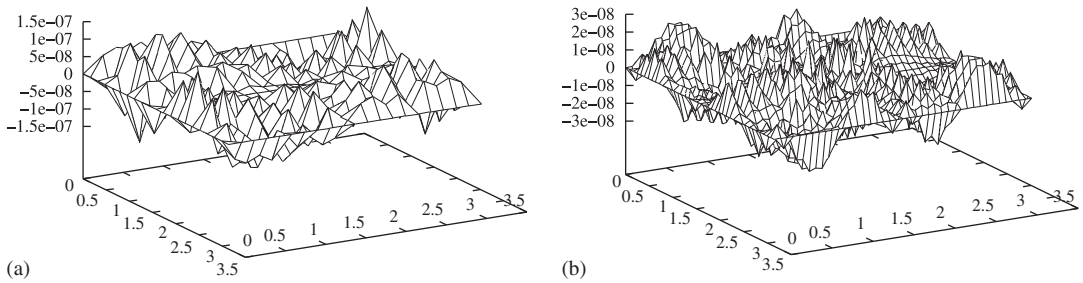

Figure 3. Problem 1: flow decayed by viscosity. Surface plots of ψ-error at time $t=5$ obtained with $\Delta t=0.01$ and grid size (a) 21×21 and (b) 41×41 for $Re=10000$.

We solved this problem using the algorithm discussed in Section 4 and used second- and fourth-order formulations for velocities given in Equations (10)–(13). Solutions were computed on grid sizes ranging from 11×11 to 41×41 with $\Delta t=0.1$ and 0.01 for various Reynolds numbers and the results are presented in Table I and Figures 1–3. In Figures 1(a) and (b), we present the exact and numerical surface and contour plots of the horizontal velocity u for $Re=1000$ at two different times $t=1$ and 500 (using $\Delta t=0.01$).

In Figure 2, we give the numerical and exact contour plots for streamfunction ψ at time $t=5$ for $Re=10000$; these solutions are obtained with a very large time step $\Delta t=0.1$ and even larger space length $\Delta x=\Delta y=\pi/10$. It is clear from these figures that the flow decays with viscosity and also that the numerical and exact plots are almost identical; one can hardly distinguish the numerical solution profiles from the analytical ones. The solutions obtained with finer grids are even more accurate, as seen in Table I.

It is worth mentioning that Strikwerda [24] found it difficult to compute solutions at high Reynolds numbers for more realistic flows, whereas our difference scheme produces remarkably accurate solutions for Re as high as 10000. This fact is also confirmed by Figure 3 where the

DOI: 10.1002/fld

Table II. Problem 2: problem with non-homogeneous source term. Convergence rates of the numerical scheme: maximum error comparisons on different grid sizes for u, v, ψ, and ω.

Grid		17×17	Rate	33×33	Rate	65×65
$t=0.25$	u_{er}	5.062×10^{-5}	1.987	1.277×10^{-5}	1.921	3.372×10^{-6}
	v_{er}	5.054×10^{-5}	1.985	1.276×10^{-5}	1.912	3.390×10^{-6}
	ψ_{er}	1.568×10^{-5}	1.989	3.957×10^{-6}	1.918	1.047×10^{-6}
	ω_{er}	2.477×10^{-2}	1.999	6.195×10^{-3}	2.000	1.549×10^{-3}
$t=1.0$	u_{er}	2.364×10^{-5}	2.012	5.863×10^{-6}	2.091	1.376×10^{-6}
	v_{er}	2.367×10^{-5}	2.006	5.891×10^{-6}	2.064	1.409×10^{-6}
	ψ_{er}	7.470×10^{-6}	2.009	1.856×10^{-6}	2.081	4.388×10^{-7}
	ω_{er}	1.170×10^{-2}	2.000	2.926×10^{-3}	2.002	7.307×10^{-4}

surface plots of ψ-errors are shown at time $t=5$ on two different grid sizes 21×21 and 41×41 for which the maximum absolute errors are extremely small, namely, 1.488×10^{-7} and 4.588×10^{-9}. The CPU times with a tolerance limit as low as 10^{-17} for the BiCGStab inner iterations were only 2.50 and 17.81 s, respectively.

In Table I, we present the maximum absolute errors on three grid sizes for the solutions computed with the fourth-order approximations for velocities given in Equations (12) and (13). Here u_{er}, v_{er}, ψ_{er} and ω_{er} are the maximum absolute errors for the horizontal velocity u, the vertical velocity v, the streamfunction ψ and vorticity ω, respectively. We also compute the numerical rates of convergence computed by the formula

$$\frac{\ln(\text{error}_1/\text{error}_2)}{\ln(h_1/h_2)}$$

where error_i is the maximum error obtained with grid of size h_i. We note that the numerical convergence rates for the velocities are of $O(h^4)$ and as expected, $O(h^2)$ for the vorticity; this convergence rate is obtained for all the values of t (see, for example $t=1$ and $t=5$). The absolute errors for the streamfunction vary from 10^{-6} to 10^{-9}. Of interest is the fact that the numerical errors for ψ converge with the rate $O(h^5)$ when the fourth-order velocity approximations are used in our computations. This rate of convergence is better than expected and may be due to the nature of the test problem being solved.

5.2. *Test problem 2*: *a problem with non-homogeneous source term*

We now consider the non-homogeneous problem in the square $0\leqslant x, y\leqslant1$

$$\nabla^4\psi-(v\nabla^2u-u\nabla^2v)=\frac{\partial}{\partial t}(\nabla^2\psi)+16\mathrm{e}^{-t}(x^2+y^2+4) \tag{24}$$

which has the analytical solution

$$\psi=\mathrm{e}^{-t}(x^2+y^2)^2$$

The solution of this problem decays rapidly as time advances. As in problem 1, the initial and boundary conditions were taken from the analytical solution. In Table II, we present maximum absolute errors for the horizontal and vertical velocities, the streamfunction and the vorticity on

DOI: 10.1002/fld

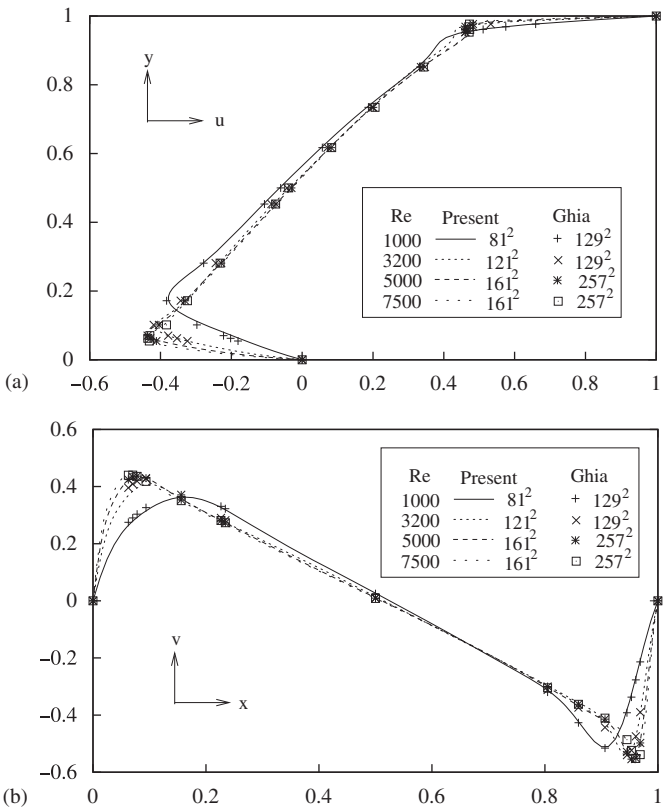

Figure 4. Comparisons of steady-state (a) horizontal velocity along the vertical centerline and (b) vertical velocity along the horizontal centerline for the lid-driven square cavity flow problem from $Re=1000$ to $Re=7500$.

three grids computed in conjunction with the fourth-order approximation of velocities given by Equations (12) and (13). This problem was considered by Ben-Artzi *et al.* [16] who presented the errors in the horizontal velocities for a variety of grids and times ranging from $t=0.25$ to $t=1$. Our data are presented in Table II and it is noted that our errors for horizontal velocities are better than the errors reported in [16]. Our errors are about one-fourth of the errors reported in [16] for $t=0.25$, and about one-tenth of the errors in [16] for $t=1$. Our errors for all the variables consistently decay with $O(h^2)$ or better rates of convergence as seen in Table II.

5.3. Test problem 3: *time evolution of lid-driven square cavity problem*

Having demonstrated the solid performance of our formulations on the exact test problems, we next consider the 2D lid-driven square cavity problem. This problem, over the years, has become the most frequently used benchmark problem for the assessment of numerical methods [1, 2, 4–11, 16], particularly for the steady-state solution of the incompressible fluid flows governed by the N–S Equations (1)–(3). This problem is of great scientific interest because it displays almost all of

DOI: 10.1002/fld

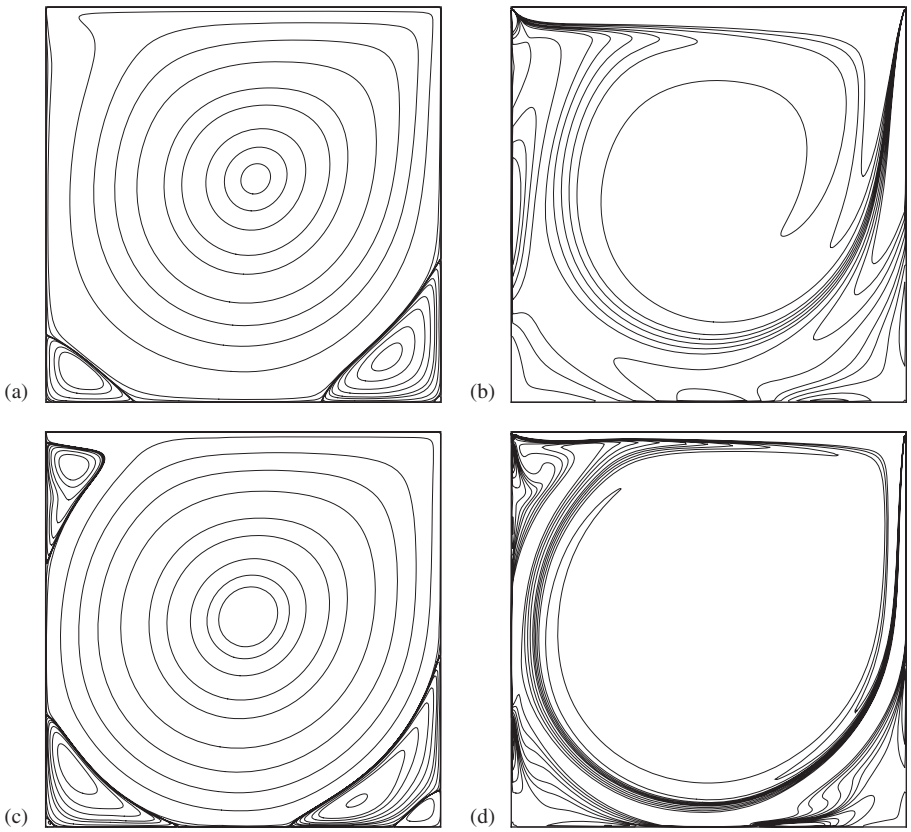

Figure 5. For the lid-driven square cavity flow problem: (a) steady-state streamlines for $Re=1000$; (b) steady-state vorticity contours for $Re=1000$; (c) steady-state streamlines for $Re=7500$; and (d) steady-state vorticity contours for $Re=7500$.

the fluid mechanical phenomena for incompressible viscous flows in the simplest of geometric settings.

The cavity is defined as the unit square $0\leqslant x, y\leqslant 1$ where the fluid motion is generated by the sliding motion of the top wall of the cavity ($y=1$) in its own plane from left to right. Boundary conditions on the top wall are given as $u=1$, $v=0$. On all other walls of the cavity the velocities are zero ($u=v=0$). Further, the streamfunction values on all four walls are zero ($\psi=0$). The moving wall generates vorticity, which diffuses inside the cavity and this diffusion is the driving mechanism of the fluid flow. At high Reynolds numbers Re, several secondary and tertiary vortices begin to appear, whose characteristics depend on the value of Re.

For our time-marching steady-state solutions of this and the next problem, the steady state was assumed to reach when the maximum ψ-error between two successive outer temporal iteration steps was smaller than 0.5×10^{-12}. Computations for the inner BiCGStab iterations were stopped when the norm of the residual vector $\bar{\mathbf{r}}=\mathbf{f}-A\boldsymbol{\psi}$ arising out of Equation (21) fell below 0.5×10^{-9}. We utilize an under-relaxation parameter λ inside the inner iteration cycles for ψ. For larger values of Reynolds number, we needed smaller values of λ.

DOI: 10.1002/fld

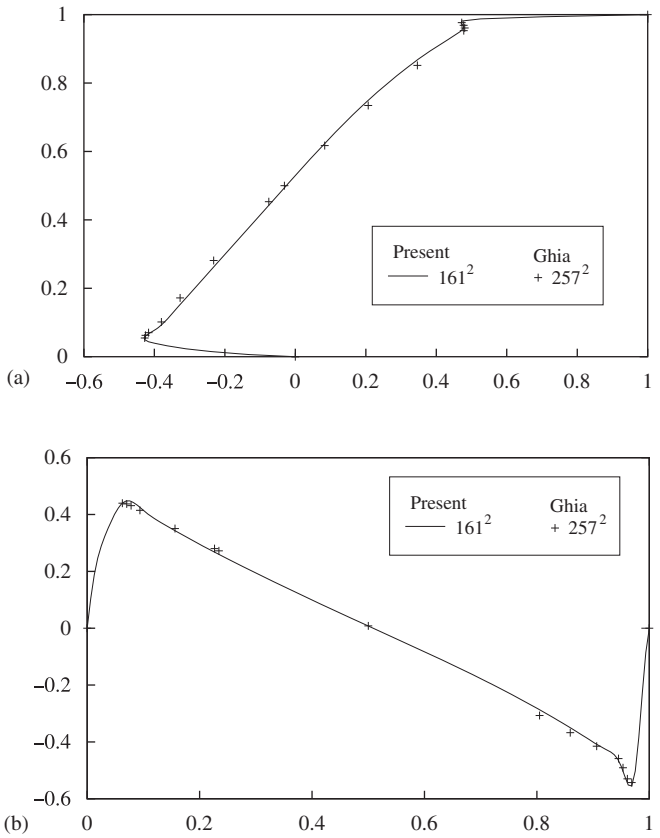

Figure 6. Comparisons of Ghia's $Re = 10000$ steady state and the present result at $t = 1361.15$ for the lid-driven square cavity flow problem: (a) horizontal velocity along the vertical centerline and (b) vertical velocity along the horizontal centerline.

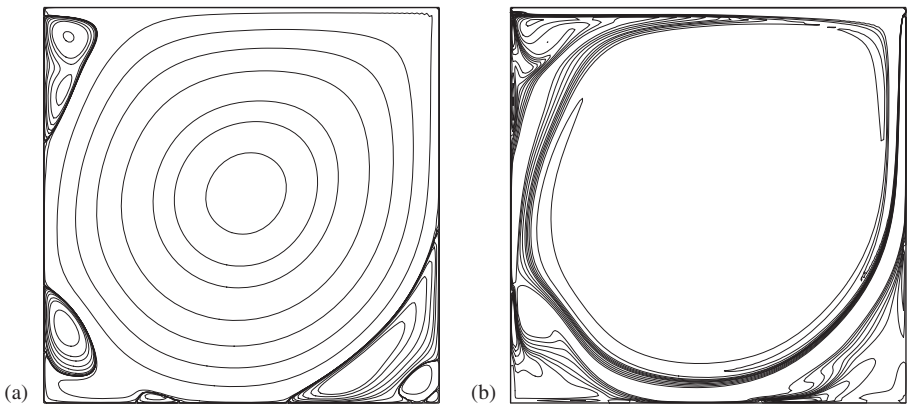

Figure 7. For the lid-driven square cavity flow problem, $Re = 10000$, at $t = 1361.15$: (a) streamlines and (b) vorticity contours.

DOI: 10.1002/fld

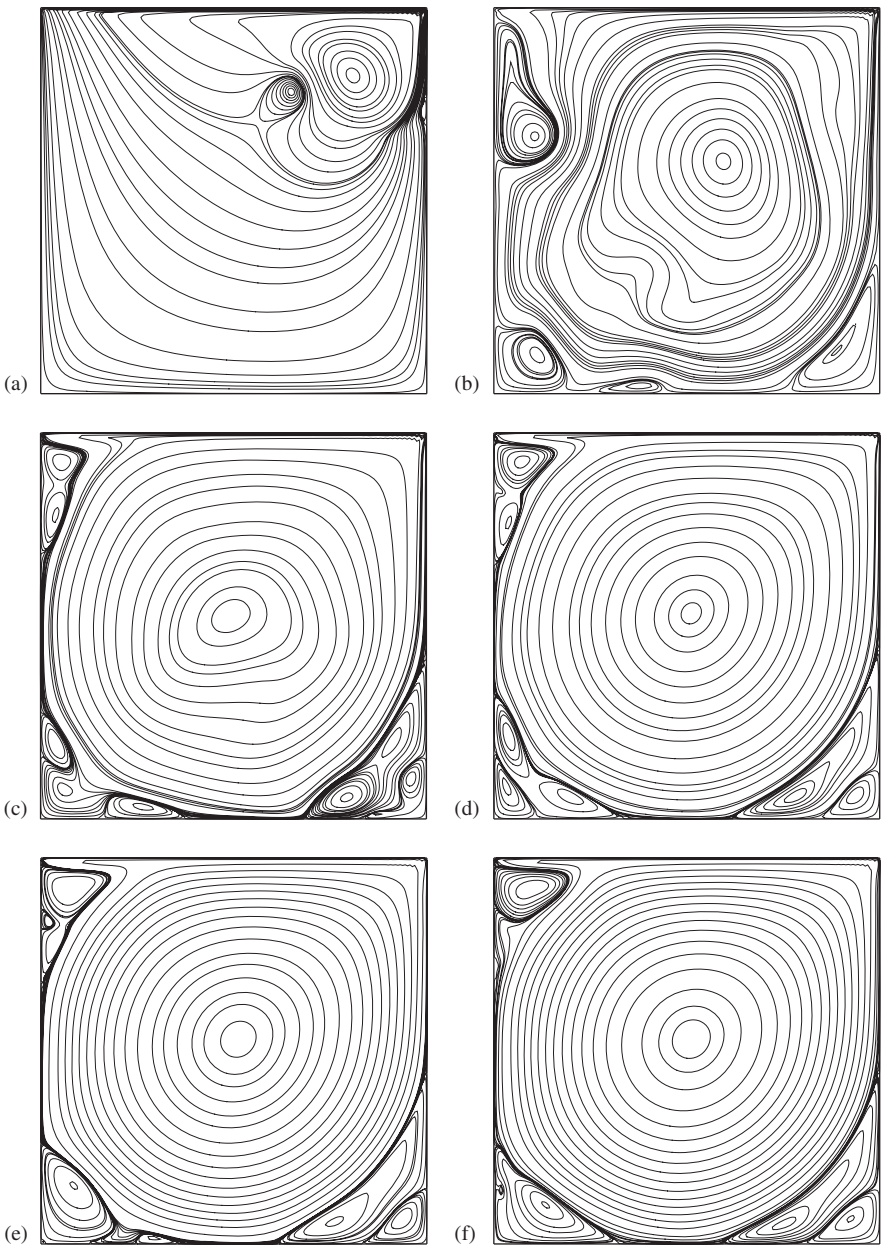

Figure 8. Evolution of streamfunction for the lid-driven square cavity flow for $Re = 10\,000$: $t =$ (a) 5; (b) 25; (c) 50; (d) 100; (e) 900 and (f) 1600.

To attain convergence for the BiCGStab iterations with Strategy 1, the value of the under-relaxation parameter λ had to be set lower than that for Strategy 2. We found that, despite having to compute ψ with an implicit formula in the corrector step, Strategy 2 is computationally more

DOI: 10.1002/fld

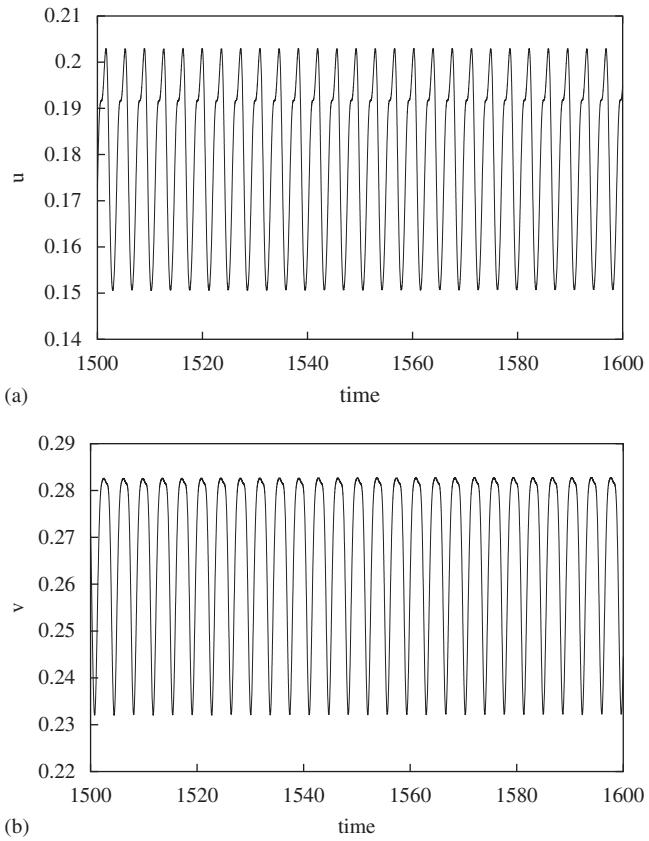

Figure 9. Computed lid-driven square cavity flow for $Re = 10000$: (a) u-velocity against time and (b) v-velocity against time at the monitoring point $\left(\frac{2}{16}, \frac{13}{16}\right)$.

economical than Strategy 1. For example, the CPU time needed for $Re = 1000$ on a 41×41 grid with Strategy 1 was 9.451 s versus 8.504 s for Strategy 2, both to complete 400 outer temporal iterations with $\Delta t = 0.025$ and a tolerance limit 0.5×10^{-6}.

In Figure 4, we present comparisons of our steady-state results of the horizontal velocities on the vertical centerline and the vertical velocities on the horizontal centerline of the square cavity for Reynolds numbers 1000 to 7500 with the steady-state data from Ghia *et al.* [7]. In each case, our velocity profiles obtained on relatively coarser grids match very well with Ghia's results. We note that all of our results, both qualitative and quantitative, including the details of the primary, secondary and tertiary vortices for the above-mentioned Reynolds numbers are very close to the results from the established References [4–8, 12]. This is also exemplified by the streamfunction and vorticity contours for $Re = 1000$ and 7500 presented in Figure 5 where we have chosen exactly the same contour values as in Reference [7]. Our computed results are almost indistinguishable from the results in [7].

We now consider our numerical results for $Re = 10000$. For this Reynolds number, we ran our code with zero initial profile on a 161×161 grid and also computed these solutions starting with

DOI: 10.1002/fld

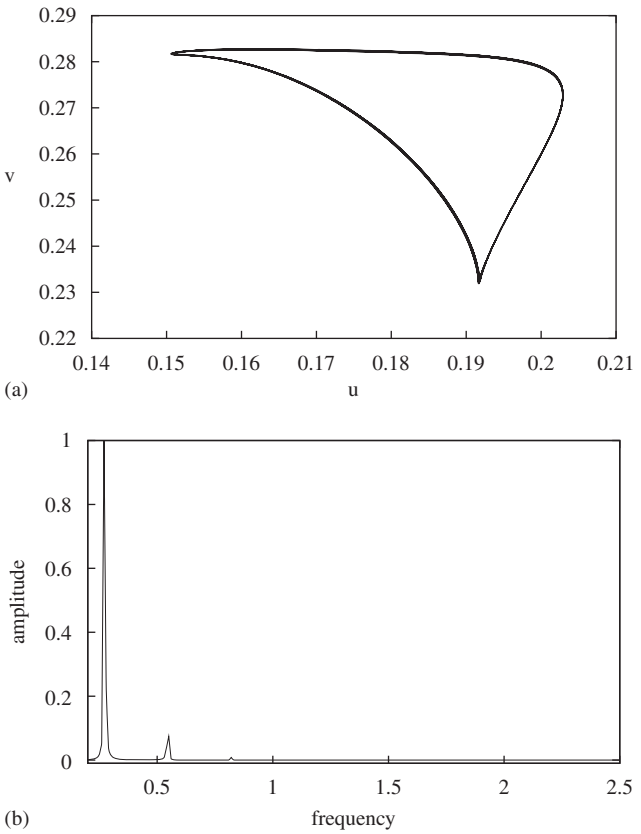

Figure 10. Computed lid-driven square cavity flow for $Re = 10000$: (a) phase-space trajectories of u versus v and (b) power spectrum of u at the monitoring point $\left(\frac{2}{16}, \frac{13}{16}\right)$.

the steady-state profiles for $Re = 7500$ as the initial data on a 257×257 grid. At time $t = 500$, the minimum and maximum values of ψ were -0.1189 and 0.0035, respectively, which are comparable to the steady-state values of -0.1197 and 0.0034 obtained by Ghia *et al.* [7]. Our primary vortex center stands at $(0.5117, 0.5312)$ against $(0.5117, 0.5333)$ of [7]. We also see in Figure 6 that at time $t = 1361.15$ on a 161×161 grid, our centerline velocity profiles match very well with those of [7].

In Figure 8, we display the evolution of the solutions for $Re = 10000$ from $t = 5$ to $t = 1600$ starting with a zero initial profile for our code. This set of profiles (along with Figure 7) clearly shows that the steady state is unstable for this value of Reynolds number. Some recent studies [12, 25, 26] have concluded that a stable steady-state solution is not possible beyond a critical Reynolds number Re_c, which is close to 8000. Our data for $Re = 10000$ support such a conclusion and lean towards an almost periodic solution. This is illustrated by the time evolution of u- and v-velocities at the monitoring point $\left(\frac{2}{16}, \frac{13}{16}\right)$ in Figure 9 and the phase plane of the u-v velocities at the same point in Figure 10(a) where the periodic nature of the solution is apparent. These figures are based on our data for $Re = 10000$ computed using 100000 time steps.

DOI: 10.1002/fld

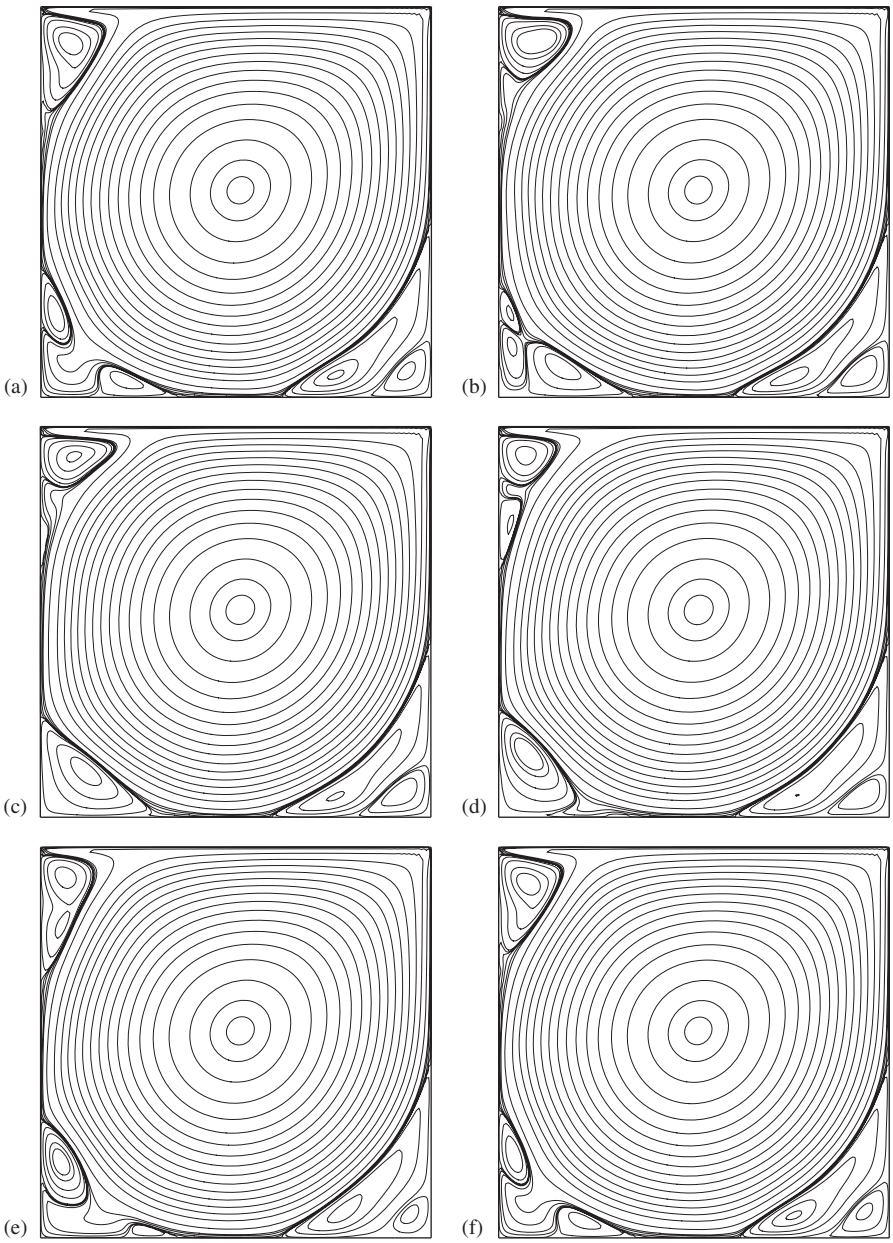

Figure 11. Evolution of streamfunction and the cyclic nature of the flow for one main period for the lid-driven square cavity flow at $Re = 10000$: $t = T_0 + \alpha$ with $T_0 = 1500$ and $\alpha =$ (a) 0; (b) 0.469; (c) 0.938; (d) 1.407; (e) 1.876 and (f) 2.345.

DOI: 10.1002/fld

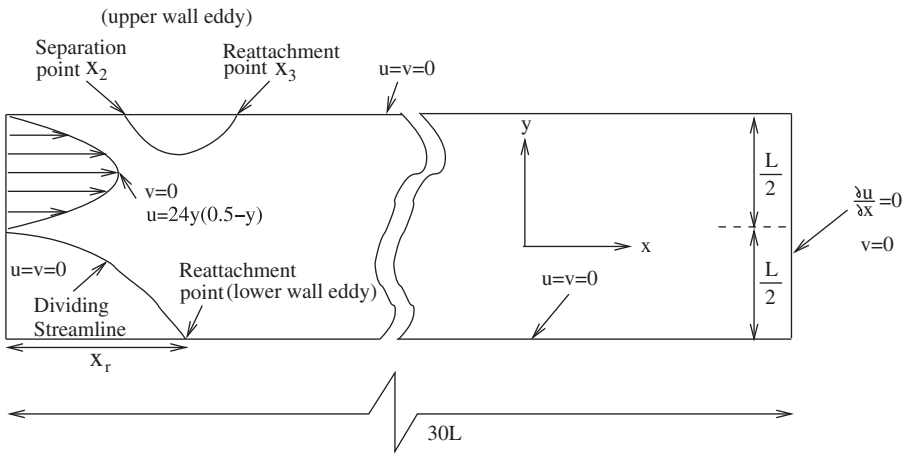

Figure 12. Configuration of the backward-facing step problem.

We also performed a Fourier analysis for the signal of u and v at different locations of the cavity as done in Reference [12]. Our analysis shows that the stable solution is mainly periodic with small variations in the amplitude of the time evolution at the monitoring points. One such plot of the power spectrum for u-velocity is exhibited in Figure 10(b).

Finally, to exhibit the global asymptotic state of the flow for $Re=10\,000$, in Figure 11, we present a sequence of six streamline contours during one main period from time $t=T_0$ to $t=T_0+2.345$ with $T_0=1500$ such that the six plots make one complete cycle. We observe that there are persistent oscillations in all of the secondary and tertiary vortices, particularly on the top left and bottom left walls while the secondary and tertiary vortices at the bottom right walls are almost stable; our observations are consistent in the findings of [12] and [26]. The periodic nature of the solution is exhibited in a movie created from data for $Re=10\,000$ from $t=1500$ to $t=1502.345$ computed using 2340 time steps (see supporting information).

5.4. Test problem 4: *the backward-facing step problem*

We now consider the flow over the backward-facing step in a channel; this example provides an excellent test case for the accuracy of our numerical method because the reattachment length is a function of the Reynolds number. Numerical simulations were carried out for Reynolds numbers 100–800 on grid sizes ranging from 601×21 to 961×33. The problem configuration is shown in Figure 12. At the inlet, a parabolic velocity profile is usually prescribed [9, 15, 27–30] and the one used here is given by Gartling [29] as $u=24y(0.5-y)$, $v=0$. The downstream boundary conditions are prescribed at a distance of 30 step heights so as to allow the flow to be fully developed. Thus at the outlet $\partial u/\partial x=0$, $v=0$ and $\partial\psi/\partial x=0$. At the stationary walls, $u=v=0$. At the outlet boundary (denoted by the index b), we approximate the values of ψ arising out of the Neumann boundary condition by the fifth-order backward difference formula (see [31]):

$$\psi_{b,j}=\frac{1}{25}\left[48\psi_{b-1,j}-36\psi_{b-2,j}+16\psi_{b-3,j}-3\psi_{b-4,j}-12h\left(\frac{\partial\psi}{\partial x}\right)_{b,j}\right]+O(h^5)$$

DOI: 10.1002/fld

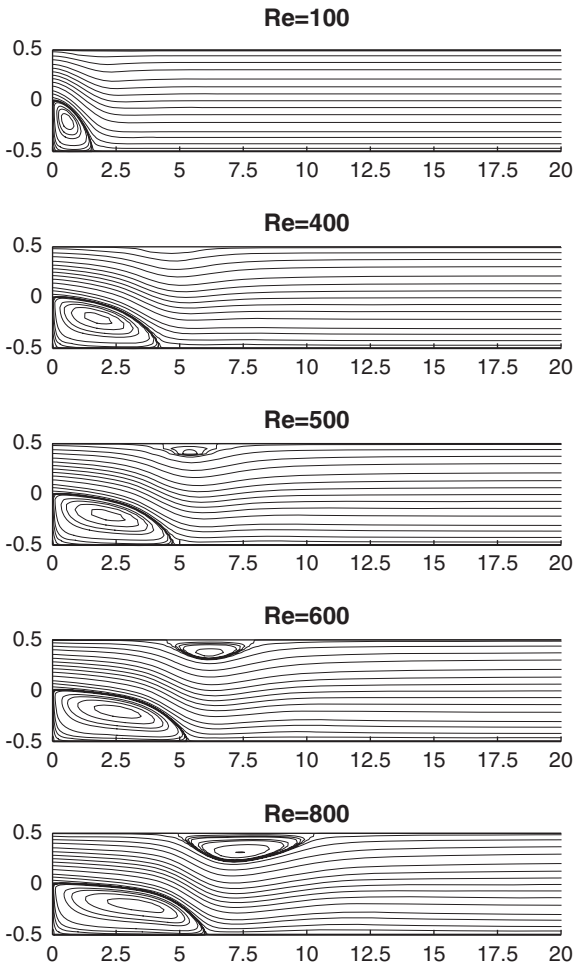

Figure 13. Steady-state streamlines for the backward-facing step flow at $Re = 100$, 400, 500, 600 and 800.

Figure 13 shows the steady-state streamline patterns for $100 \leqslant Re \leqslant 800$. One can see a steady increase in the reattachment length with the increase in Re. The formation of a secondary vortex at the upper wall can be seen from $Re = 500$ onwards; this was also reported by Sohn [28]. In Figure 14, we show the horizontal velocity profiles for $Re = 600$ at two locations $x = 7$ and $x = 15$ on 601×21 and 961×33 grids which confirm the grid independence of the computed solutions for this value of Re.

In Figure 15, we present the streamwise velocity profiles for $Re = 800$ at $x = 7$ and compare our results with those of Gartling [29] and Keskar and Lyn [32]. It is clear that our solution profiles show an excellent match with the published results. In Figure 16, we exhibit the velocity vector plots of the steady-state solutions for $100 \leqslant Re \leqslant 800$. These velocity vector plots give a clear picture of the recirculation zones and the velocity profiles at different streamwise locations, and also indicate the development of a parabolic profile towards the exit. Note that, in these figures, we have magnified the spacing in the y-direction four times for a better resolution.

DOI: 10.1002/fld

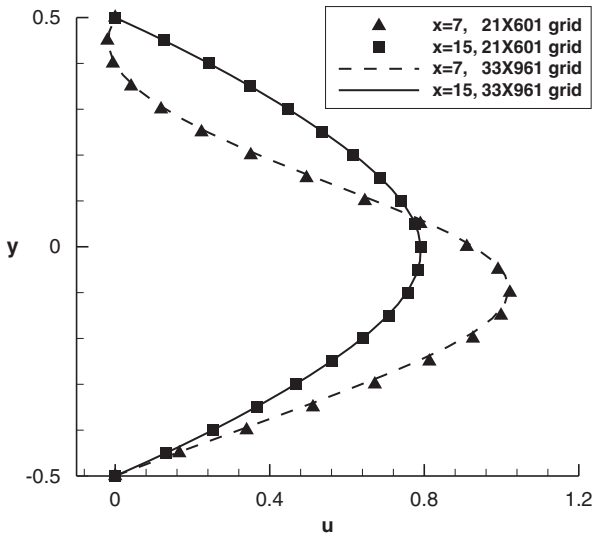

Figure 14. Grid independence study for the horizontal velocity profiles for $Re = 600$ at $x = 7$ and $x = 15$ on grids of sizes 601×21 and 961×33.

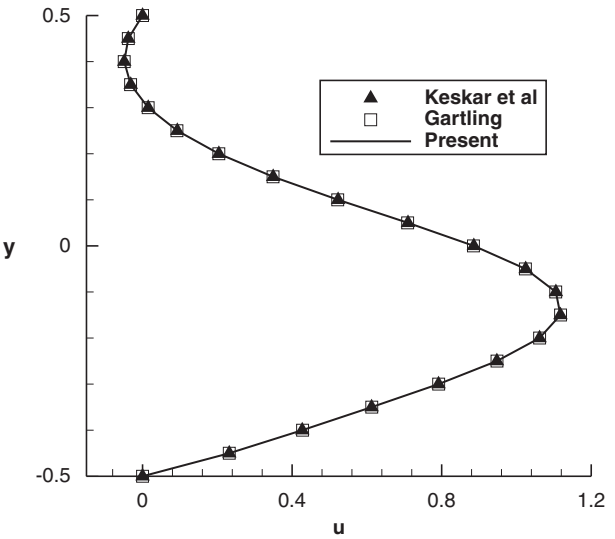

Figure 15. Comparison of the horizontal velocity profiles for $Re = 800$ at $x = 7$ with the results of [32] and [29].

In Table III, we present lower and upper wall eddy data and compare them with the available results [15, 29, 30, 32, 33]. Though there are not many quantitative results in the literature for lower values of Re, there are many published results for $Re = 800$. In each case, the results obtained with our streamfunction–velocity formulation are very accurate and match the published data very well.

DOI: 10.1002/fld

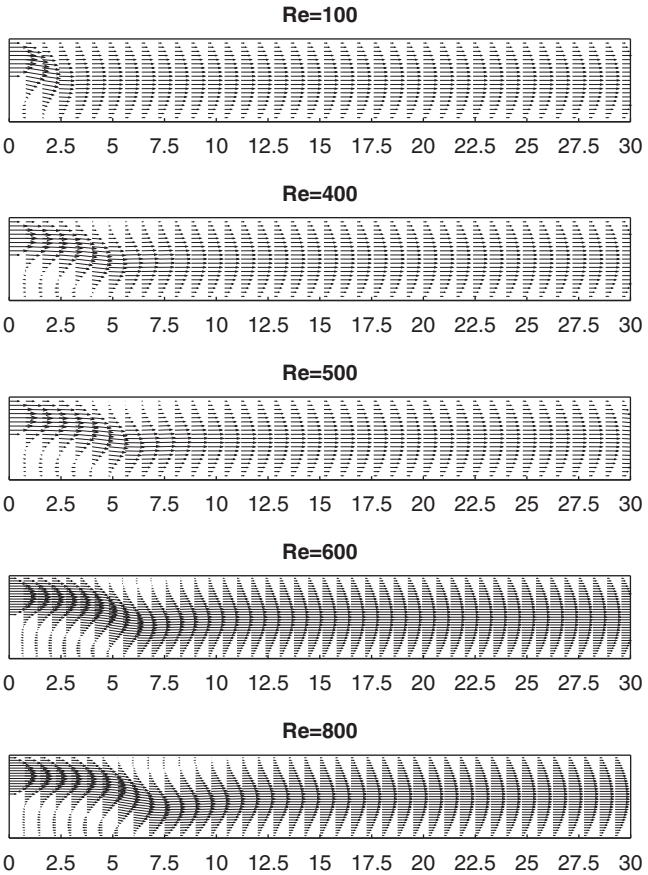

Figure 16. Steady-state relative vector velocity plots for the backward-facing step flow at $Re = 100$, 400, 500, 600 and 800.

In Figure 17, we show the time evolution of the streamlines for $Re = 600$. One can see the development of the main vortices at the step and on the top wall; a secondary vortex appears at the bottom left corner starting at $t = 10$. After a while (as seen at $t = 17$ and 25), two smaller vortices begin appearing at the top and bottom walls; these vortices diffuse completely before the steady state is reached. The main vortex at the top wall splits into two vortices (see the figure at $t = 25$) and within a short period of time these vortices coalesce into one vortex (see the figure at $t = 29$). Both of the main vortices grow in size with time. Once the steady state is reached, only the vortices at the top wall, at the step and the secondary vortex at the bottom left corner (not visible in the figures) continue to exist (see also Figure 13 for $Re = 600$).

In Figure 18, we exhibit the reattachment length as a function of the Reynolds number, and compare it with the experimental and computational results of Armaly *et al.* [27] and the numerical results of Kim and Moin [9]. As these authors have not provided quantitative data, we scanned their graphical results in order to produce the cited quantities. As seen in Figure 18, Our results are

DOI: 10.1002/fld

Table III. Properties of wall eddy for the backward-facing step problem from $Re=400$ to $Re=800$.

Wall	Re	400	500	600	800
Lower	Eddy center (x, y)	(1.750, −0.200)	(2.150, −0.200)	(2.438, −0.200)	(3.525, −0.218)
		(1.705, −0.188) [15]	(2.079, −0.1874) [15]	(2.438, −0.188) [15]	(3.500, −0.219) [15]
		(1.800, −0.200) [34]	(2.199, −0.200) [34]		(3.350, −0.200) [29]
	ψ_{value}	−0.03326	−0.03328	−0.03370	−0.03374
		(−0.03364) [15]	(−0.03373) [15]	(−0.03375) [15]	(−0.03381) [15]
		(−0.03412) [34]	(−0.03463) [34]		(−0.0342) [29]
					(−0.0342) [32]
	Recirculation	4.200	4.750	5.313	6.031
	Length	(4.239) [15]	(4.853) [15]	(5.319) [15]	(6.000) [15]
		(4.32) [30]	(5.16) [33]	(5.50) [30]	(6.22) [30]
					(6.097) [32]
					(6.10) [29]
Upper	Eddy center (x, y)	—	(5.400, 0.400)	(6.175, 0.375)	(7.375, 0.313)
			(5.438, 0.406) [15]	(6.170, 0.375) [15]	(7.385, 0.313) [15]
			(5.400, 0.413) [34]		
	ψ_{value}	—	0.5006	0.5023	0.5065
			(0.5005) [15]	(0.5023) [15]	(0.5066) [15]
			(0.5005) [34]		(0.5065) [32]
	Separation	—	4.163	4.468	4.876
	Point x_2		(4.309) [15]	(4.505) [15]	(4.897) [15]
			(4.255) [34]	(4.13) [33]	(4.28) [33]
					(4.70) [28]
					(5.13) [30]
					(4.85) [29]
					(4.85) [32]
	Reattachment	—	6.613	7.969	10.312
	Point x_3		(6.555) [15]	(7.908) [15]	(10.279) [15]
			(6.358) [34]	(7.83) [33]	(9.28) [33]
					(9.40) [28]
					(10.22) [30]
					(10.48) [29]
					(10.48) [32]

DOI: 10.1002/fld

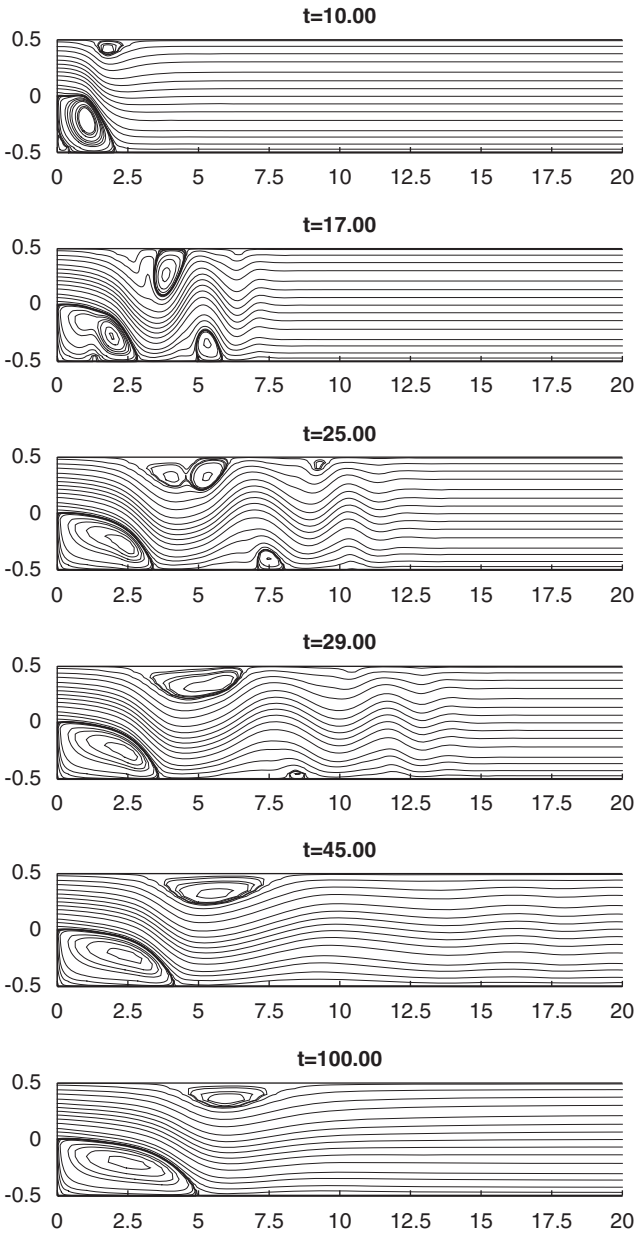

Figure 17. Streamline evolution for the backward-facing step flow at $Re=600$ at time stations $t=10$, 17, 25, 29, 45 and 100 s.

in excellent agreement with the experimental results of Armaly *et al.* [27] for $100 \leqslant Re \leqslant 500$. The discrepancy between the numerical and experimental results of [27] for $Re \geqslant 600$ may be attributed to the three-dimensionality effects associated with the latter [9, 29, 35, 36].

DOI: 10.1002/fld

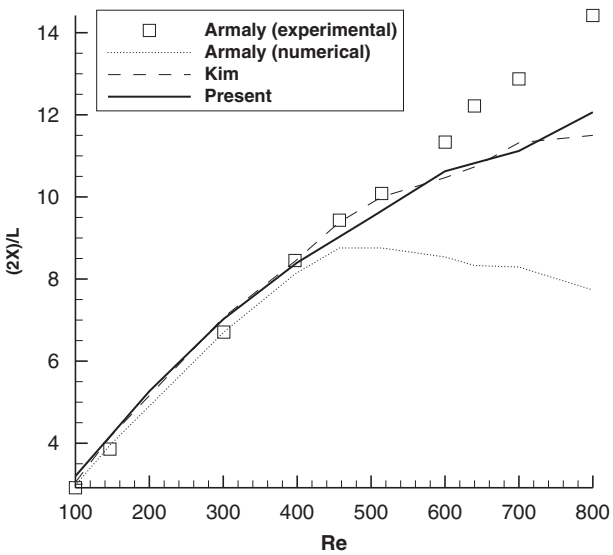

Figure 18. The reattachment length as a function of Reynolds number.

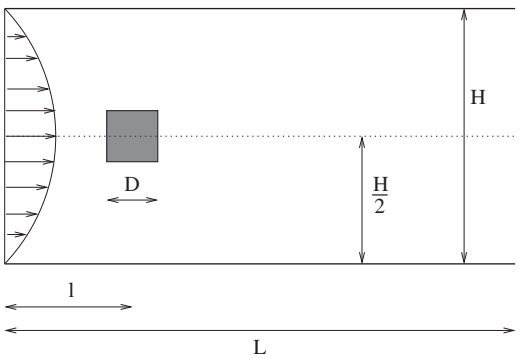

Figure 19. Configuration of the flow past a square cylinder problem.

5.5. *Test problem 5*: *flow past a square prism*

As our final test problem, we solved the problem of flow past a square prism. The domain of the flow is multiply connected and the nature of the flow itself is very complex. The unsteady behavior of the flow that evolves with time for Reynolds numbers beyond a critical value makes this problem more challenging and interesting. Thus this problem serves as a suitable test case to check the robustness and reliability of the proposed numerical scheme.

The problem configuration is similar to the one by Breuer *et al.* [37] as shown in Figure 19: it has a cylinder with square cross-section (square prism) with diameter (width) D mounted and centered inside a plane channel of height H with blockage ratio $B=\frac{1}{8}$. The channel length L

DOI: 10.1002/fld

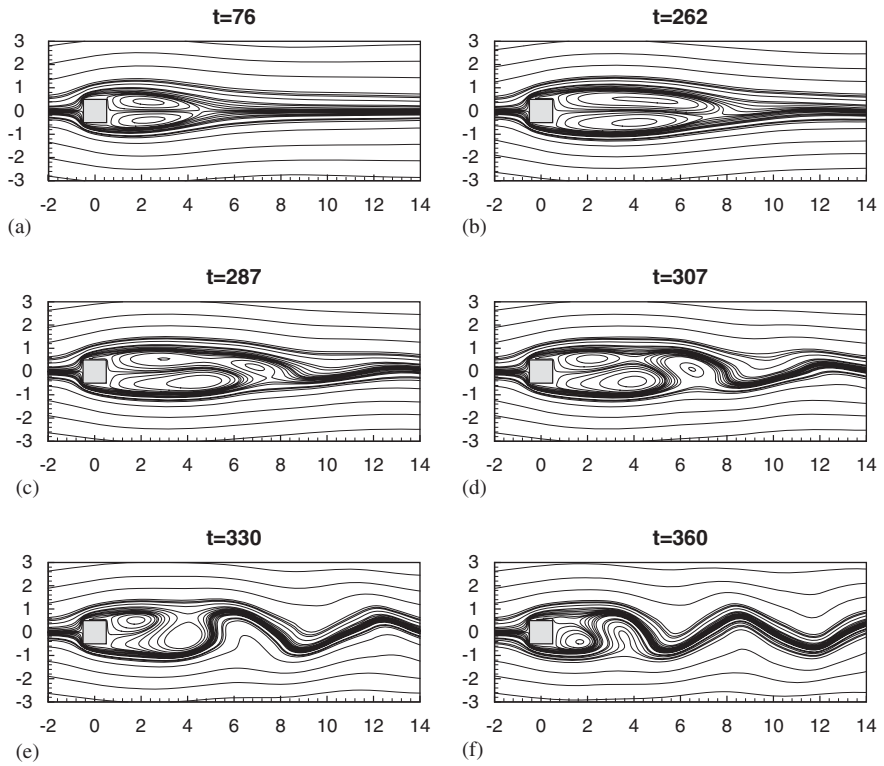

Figure 20. Evolution of streamfunction towards a periodic state for the flow past a square prism problem at $Re=200$: (a) $t=76$; (b) $t=262$; (c) $t=287$; (d) $t=307$; (e) $t=330$; and (f) $t=360$.

was fixed at $\frac{L}{D}=50$ to reduce the influence of inflow and outflow boundary conditions. An inflow length of $l=\frac{L}{4}$ was chosen. At the inlet, a parabolic profile was introduced while at the outlet, convective boundary conditions given by

$$\frac{\partial \phi}{\partial t}+u_{\text{conv}}\frac{\partial \phi}{\partial x}=0 \tag{25}$$

was used with ϕ standing for u, v or ψ. Here u_{conv} was set equal to the maximum u-velocity of the inlet. No-slip boundary conditions were applied on the surface of the square prism and on both the upper and lower boundaries.

The main goal of this study was to test the robustness of the proposed scheme rather than to study the flow past a square prism. To numerically simulate the quantitative and qualitative fluid flow features, we focus on a chosen Reynolds number value of 200; we note that we are able to accurately capture the characteristics of the flow using a uniform grid of size 161×1001, whereas other authors [35, 37, 38] had to resort to either parallel computing, dividing the solution domain into multi-blocks or clustering near the surface of the cylinder on larger computational grids.

DOI: 10.1002/fld

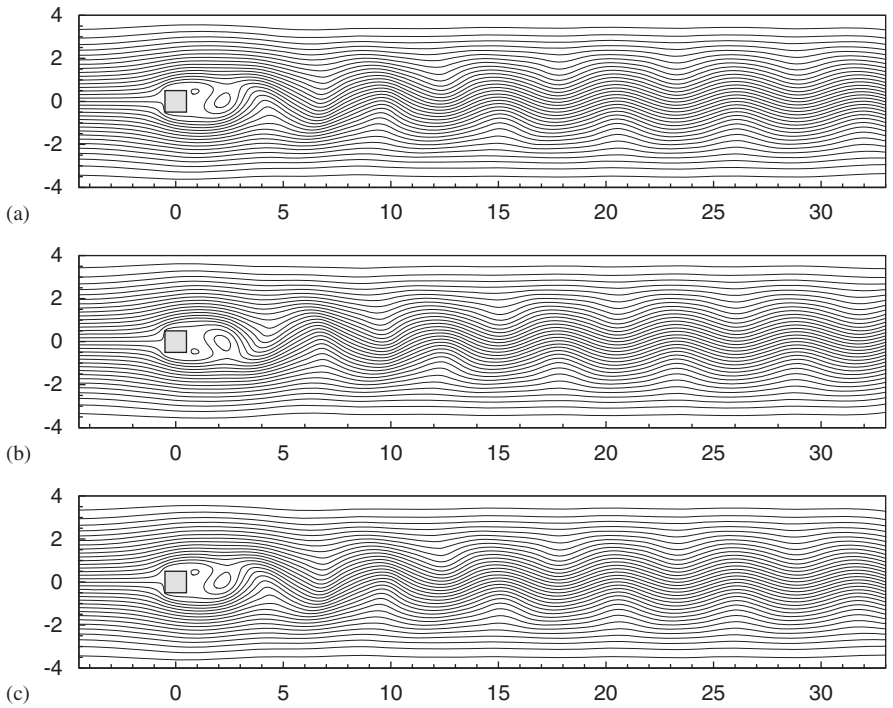

Figure 21. The streamfunction contours depicting the wake behind three successive instants of time over one vortex shedding period: (a) $t = t_0$; (b) $t = t_0 + \frac{T}{2}$ and (c) $t = t_0 + T$.

In our computations, we used the uniform flow parameters as initial conditions and present the solution profiles in Figure 20 for various values of t. As seen in Figure 20, a symmetric flow was observed at the beginning (Figure 20(a)), but the flow became unstable later on, and finally the flow lost its symmetry (Figures 20(b)–(e)). Eventually, the flow settled into a periodic nature (Figure 20(f)). We present the temporal evolution of streamlines and vorticity over one complete vortex shedding cycle of duration T in Figures 21 and 22. The evolution of an impressive von Kármán vortex street, which is a regular feature of the Reynolds number considered here, is clearly seen in these figures.

From Figure 21, one can see the formation of eddies just behind the square prism; these eddies are then washed away into the wake region. Two eddies are shed just behind the cylinder within each period (see also Figures 20(f) and 23(a)). Figures 21(a) and 21(b) are half a vortex shedding cycle apart, and the middle Figure 21(b) is a mirror image of Figures 21(a) and 21(c). The periodic nature of the sequence is apparent from Figures 21(a)–(c). The corresponding vorticity contours are depicted in Figures 22(a)–(c). Several features of the flow, that are not directly obvious from the streamlines, are revealed by these vorticity contours. The staggered nature of the Kármán shedding is clear from these plots. The crests and troughs of the sinuous waves in the streamlines reflect the alternatively positive and negative vorticities of the eddies. To depict the activities behind the wake more clearly, we present a close-up view of the streamlines and the vorticity contours in Figure 23.

DOI: 10.1002/fld

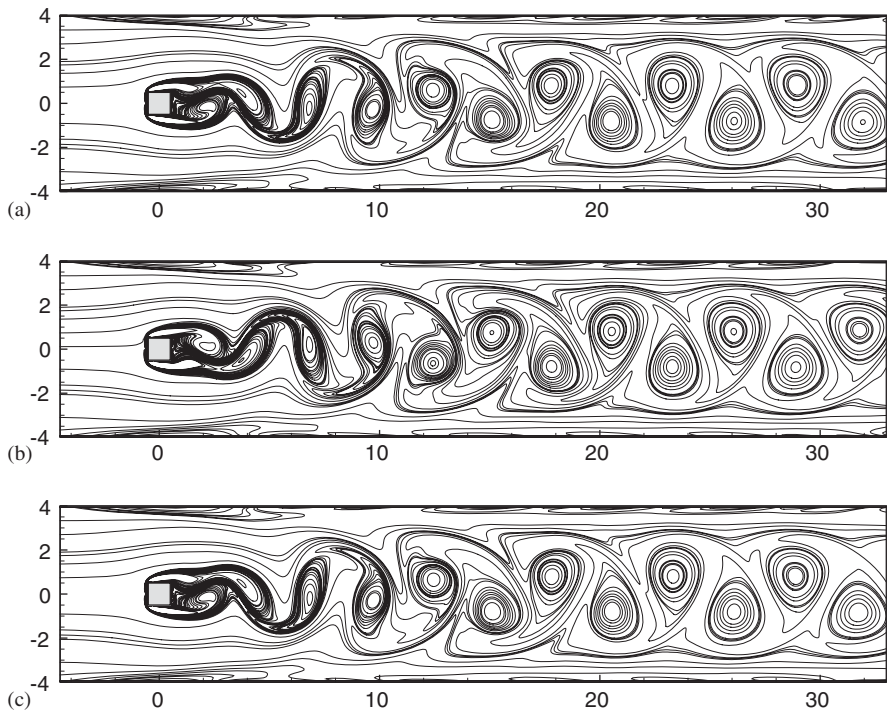

Figure 22. The vorticity contours depicting the wake behind three successive instants of time over one vortex shedding period: (a) $t=t_0$; (b) $t=t_0+\frac{T}{2}$ and (c) $t=t_0+T$.

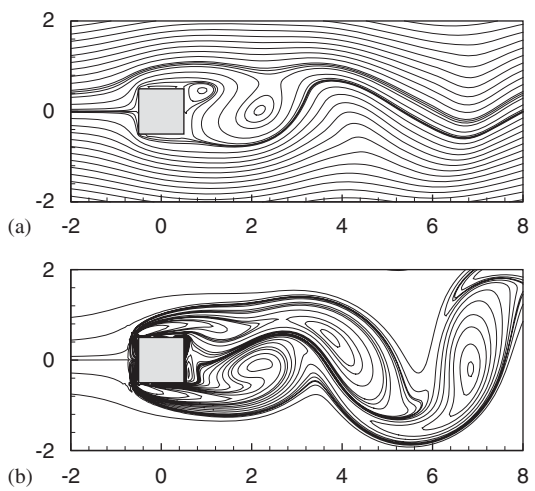

Figure 23. A close-up view of the flow patterns for the motion past a square prism problem: (a) streamlines and (b) vorticity contours.

DOI: 10.1002/fld

6. CONCLUSION

In this paper, we present an implicit unconditionally stable streamfunction–velocity formulation for the unsteady two-dimensional (2D) Navier–Stokes equations. The scheme is second-order accurate, both temporally and spatially. It is easy to implement and the use of BiCGStab algorithm, for solving the algebraic systems at each time level, makes the implicit procedure computationally efficient for capturing the transient solutions. To highlight the different aspects of our scheme, we used it to compute the transient solutions of two problems where the exact solutions are known; we also solved the time-dependent 2D lid-driven cavity flow and the backward-facing step flow problem to obtain their time-marching steady solutions.

The robustness of our scheme is illustrated by its applicability to a wide range of problems of varying physical complexities, represented by Reynolds numbers ranging from 100–10 000. Computational efficiency of the present scheme is reflected in very low demand on the CPU time. The results obtained in all of the test cases are in excellent agreement with the available analytical as well as experimental and numerical results, which underline the high accuracy of our scheme.

The implicit nature of our scheme is fully exploited in reaching the steady-state results for the lid-driven cavity and the backward step problems, and also time accurate transient solution for the viscosity problem where we used time steps as large as 0.1 for many of the computations. Finally, robustness of the scheme is highlighted when it captures the almost periodic nature of the asymptotic solutions for $Re=10\,000$ in the lid-driven cavity flow, and even more so for the laminar flow past a square prism with $Re=200$ where we successfully simulated the von Kármán street behind the square prism. This clearly indicates that our scheme can accurately capture incompressible viscous flows on rectangular geometries containing multiply connected regions as well.

Because of its high computational efficiency, our scheme has a good potential for efficient application to many more problems and our method is an important addition to the high accuracy solution procedures for transient incompressible viscous flows. Currently we are working on the parallel implementation and expansion of the code to curvilinear coordinates and preliminary indications are that this would be very successful.

APPENDIX A

A.1. Extension of the current scheme to three dimensions

The unsteady N–S equations for incompressible viscous flows in 3D is given by

$$\frac{\partial \vec{u}}{\partial t}+(\vec{u}\cdot\nabla)\vec{u}-\frac{1}{Re}\nabla^2\vec{u}=-\nabla p \tag{A1}$$

where $\vec{u}$ is the 3D velocity vector, Re is the Reynolds number given by $Re=Lu_0/v$ with L being a characteristic length, u_0 some characteristic velocity and v the kinematic viscosity.

Taking the curl of both the sides of (A1), we obtain the 3D vorticity equation of the form

$$\frac{\partial \boldsymbol{\omega}}{\partial t}+(\vec{u}\cdot\nabla)\boldsymbol{\omega}-(\boldsymbol{\omega}\cdot\nabla)\vec{u}=\frac{1}{Re}\nabla^2\boldsymbol{\omega} \tag{A2}$$

DOI: 10.1002/fld

with $\boldsymbol{\omega}=\nabla\times\vec{u}$. Introducing the 3D streamfunction vector $\boldsymbol{\psi}$, given by $\vec{u}=\nabla\times\boldsymbol{\psi}$ such that $\boldsymbol{\omega}=\nabla\times(\nabla\times\boldsymbol{\psi})=\nabla(\nabla\cdot\psi)-\nabla^2\boldsymbol{\psi}=-\nabla^2\boldsymbol{\psi}$, Equation (A2) yields

$$\frac{\partial}{\partial t}(\nabla^2\boldsymbol{\psi})+[(\nabla\times\boldsymbol{\psi})\cdot\nabla]\nabla^2\boldsymbol{\psi}-(\nabla^2\boldsymbol{\psi}\cdot\nabla)(\nabla\times\boldsymbol{\psi})=\frac{1}{Re}\nabla^4\boldsymbol{\psi} \tag{A3}$$

In Reference [39], Altas *et al.* have proposed a compact finite difference scheme for numerically solving the 3D biharmonic equations of the form

$$\nabla^4\phi(x,y,z)=f(x,y,z) \tag{A4}$$

Now, each of the three components of (A3) can be put in the form

$$\frac{1}{Re}\nabla^4\phi=\frac{\partial}{\partial t}(\nabla^2\phi)+f(x,y,z) \tag{A5}$$

which is exactly of the form (A4) except for the time derivative term. In conjunction with the existing scheme in Reference [39] and the strategy adopted to develop the current scheme for 2D transient N–S equation in biharmonic form as described in Section 2, a compact finite difference scheme could be developed for the 3D N–S equations as well. We shall discuss the details of this scheme in a separate paper in the near future.

REFERENCES

1. Kalita JC, Dalal DC, Dass AK. A class of higher order compact schemes for the unsteady two-dimensional convection-diffusion equation with variable convection coefficients. *International Journal for Numerical Methods in Fluids* 2002; **38**:1111–1131.
2. Kalita JC, Dass AK, Dalal DC. A transformation-free HOC for steady convection–diffusion on nonuniform grids. *International Journal for Numerical Methods in Fluids* 2004; **44**:33–53.
3. Chen Y-N, Yang S-C, Yang J-Y. Implicit weighted essentially non-oscillatory schemes for the incompressible Navier–Stokes equations. *International Journal for Numerical Methods in Fluids* 1999; **31**:747–765.
4. Barragy E, Carey GF. Streamfunction–vorticity driven cavity solution using p finite elements. *Computers and Fluids* 1997; **26**:453–468.
5. Botella O, Peyret R. Benchmark spectral results on the lid-driven cavity flow. *Computers and Fluids* 1998; **27**:421–433.
6. Bruneau C-H, Jouron C. An efficient scheme for solving steady incompressible Navier–Stokes equations. *Journal of Computational Physics* 1990; **89**:389–413.
7. Ghia U, Ghia KN, Shin CT. High Re-solution for incompressible Navier–Stokes equation and a multigrid method. *Journal of Computational Physics* 1982; **48**:387–411.
8. Hou S, Zou Q, Chen S, Doolen G, Cogley A. Simulation of cavity flows by the lattice Boltzmann method. *Journal of Computational Physics* 1995; **118**:329–347.
9. Kim J, Moin P. Application of fractional step method to incompressible Navier–Stokes equation. *Journal of Computational Physics* 1985; **59**:308–323.
10. Schreiber R, Keller HB. Driven cavity flows by efficient numerical techniques. *Journal of Computational Physics* 1983 **49**:310–333.
11. Vanka SP. Block-implicit multigrid solution of Navier–Stokes equations in primitive variables. *Journal of Computational Physics* 1986; **65**:138–158.
12. Bruneau C-H, Saad M. The 2D lid-driven cavity problem revisited. *Computers and Fluids* 2005; **35**(3):326–348.
13. Chorin AJ. Numerical solutions of the Navier–Stokes equations. *Mathematics of Computation* 1968; **95**:745–762.
14. Gupta MM, Kalita JC. A new paradigm for solving Navier–Stokes equations: streamfunction–velocity formulation. *Journal of Computational Physics* 2005; **207**(1):52–68.
15. Gupta MM, Kalita JC. New paradigm continued: further computations with streamfunction–velocity formulation for solving Navier–Stokes equations. *Communications in Applied Analysis* 2006; **10**(4):461–490.

DOI: 10.1002/fld

16. Ben-Artzi M, Croisille J-P, Fishelov D, Trachtenberg S. A pure-compact scheme for the streamfunction formulation of Navier–Stokes equations. *Journal of Computational Physics* 2005; **205**(2):640–664.
17. Fishelov D, Ben-Artzi M, Croisille J-P. *A Compact Scheme for the Streamfunction Formulation of Navier–Stokes Equations*. Notes on Computer Sciences, vol. 2667. Springer: Berlin, 2003; 809–817.
18. Kupferman R. A central difference scheme for a pure streamfunction formulation of incompressible viscous flow. *SIAM Journal on Scientific Computing* 2001; **23**(1):1–18.
19. Chung TJ. *Computational Fluid Dynamics*. Cambridge University Press: Cambridge, 2003.
20. Kelley CT. *Iterative Methods for Linear and Nonlinear Equations*. SIAM Publications: Philadelphia, 1995.
21. Saad Y. *Iterative Methods for Sparse Linear Systems*. PWS Publishing Company: Boston, 1996.
22. Sleijpen GLG, van der Vorst HA. Hybrid biconjugate methods for CFD problems. In *Computational Fluid Dynamics Review*, Hafez M, Oshima K (eds). John Wiley & Sons Ltd.: Chichester, 1995; 457–476.
23. van der Vorst H. BiCGSTAB: a fast and smoothly converging variant of BiCG for the solution of nonsymmetric linear systems. *SIAM Journal on Scientific Computing* 1992; **13**:631–644.
24. Strikwerda JC. High-order accurate schemes for incompressible viscous flow. *International Journal for Numerical Methods in Fluids* 1997; **24**:715–734.
25. Peng Y-F, Shiau Y-H, Hwang RR. Transition in a 2D lid-driven cavity flow. *Computers and Fluids* 2003; **32**:337–352.
26. Shen J. Hopf bifurcation of the unsteady regularized driven cavity. *Journal of Computational Physics* 1991; **95**:228–245.
27. Armaly BF, Durst F, Pereira J, Schonung B. Experimental and theoretical investigation of backward facing step flow. *Journal of Fluid Mechanics* 1983; **127**:473–496.
28. Sohn J. Evaluation of FIDAP on some classical laminar and turbulent benchmarks. *International Journal for Numerical Methods in Fluids* 1988; **8**:1469–1490.
29. Gartling DK. A test problem for outflow boundary conditions-flow over a backward facing step. *International Journal for Numerical Methods in Fluids* 1990; **11**:953–967.
30. Srinivasan K, Rubin SG. Segmented multigrid domain decomposition procedure for incompressible viscous flows. *International Journal for Numerical Methods in Fluids* 1992; **15**:1333–1355.
31. Anderson DA, Tannehil JC, Pletcher RH. *Computational Fluid Mechanics and Heat Transfer*. Hemisphere Publishing Corporation: New York, 1984.
32. Keskar J, Lyn DA. Computations of a laminar backward-facing step flow at $Re = 800$ with a spectral domain decomposition method. *International Journal for Numerical Methods in Fluids* 1999; **29**:411–427.
33. Barton IE. A numerical study of flow over a confined backward step. *International Journal for Numerical Methods in Fluids* 1995; **21**:653–665.
34. Kalita JC, Sen S. The $(9, 5)$ HOC formulation for the transient Navier–Stokes equations in primitive variable. *International Journal for Numerical Methods in Fluids* 2007; **55**:387–406.
35. Wan DC, Patnaik BS, Wei GW. Discrete singular convolution-finite subdomain method for the solution of incompressible viscous flows. *Journal of Computational Physics* 2002; **180**:229–255.
36. Zhu JY. The 2nd order projection method for the backward-facing step flow. *Journal of Computational Physics* 1995; **117**:318–331.
37. Breuer M, Bernsdorf J, Zeiser T, Durst F. Accurate computations of the laminar flow past a square cylinder based on two different methods: lattice-Boltzmann and finite-volume. *International Journal of Heat and Fluid Flow* 2000; **21**:186–196.
38. Abide S, Viazzo S. A 2D compact fourth-order projection decomposition method. *Journal of Computational Physics* 2005; **206**:252–276.
39. Altas I, Erhel J, Gupta MM. High accuracy solution of three-dimensional biharmonic equations. *Numerical Algorithms* 2002; **29**:1–19.

DOI: 10.1002/fld